The Role of Contact Line (Pinning) Forces on Bubble Blockage in Microchannels

Citation	Mohammadi, M., & Sharp, K. V. (2015). The Role of Contact Line (Pinning) Forces on Bubble Blockage in Microchannels. Journal of Fluids Engineering – Transactions of the ASME, 137(3), 031208. doi:10.1115/1.4029033.
DOI	10.1115/1.4029033
Publisher	The American Society of Mechanical Engineers (ASME)
Version	Accepted Manuscript
Terms of Use	http://cdss.library.oregonstate.edu/sa-termsofuse

The Role of Contact Line (Pinning) Forces on Bubble Blockage in Microchannels

Mahshid Mohammadi

E-mail: mahshid@lifetime.oregonstate.edu

Kendra V. Sharp

E-mail: kendra.sharp@oregonstate.edu

204 Rogers Hall, Oregon State University, Corvallis, OR 97331

Abstract

This paper highlights the influence of contact line (pinning) forces on the mobility of dry bubbles in microchannels. Bubbles moving at velocities less than the dewetting velocity of liquid on the surface are essentially dry, meaning that there is no thin liquid film around the bubbles. For these "dry" bubbles, contact line forces and a possible capillary pressure gradient induced by pinning act on the bubbles and resist motion. Without sufficient driving force (e.g. external pressure) a dry bubble is brought to stagnation. For the first time, a bipartite theoretical model that estimates the required pressure difference across the length of stagnant bubbles with concave and convex back interfaces to overcome the contact line forces and stimulate motion is proposed. To validate our theory, the pressure required to move a single dry bubble in square microchannels exhibiting contact angle hysteresis has been measured. The working fluid was deionized water. The experiments have been conducted on coated glass channels with different surface hydrophilicities that resulted in concave and convex back interfaces for the bubbles. The experimental results were in agreement with the model's predictions for square channels. The predictions of the concave and convex back models were within 19% and 27% of the experimental measurements, respectively.

1 Introduction

Bubble clogging in microchannels is a well-known problem in microfluidics. Immobile bubbles induce strong resistance effects on the flow in the channels and may disturb the performance and reduce the efficiency of the device [1]. Therefore, management of gas bubbles is an important matter for microfluidic devices. The emergence of the bubbles can be caused by various factors, e.g., simply by diffusion of air into the device or by the degassing of the liquid due to temperature or pressure variations. Vibration can stimulate the formation of the bubbles as well [2]. Bubbles can also get introduced into the system while connecting or disconnecting tubing to the valves, pumps, etc. Overall, in practice, the chances of the appearance of unwanted bubbles in microfluidic devices are relatively high. Furthermore, bubbles may be generated as a reaction product in the device, e.g. the production of carbon dioxide during the oxidation of methanol on the anode side of a micro direct methanol fuel cell (μDMFC) [3]. Two-phase micro-heat exchangers may also experience bubble removal problems [4-6]. In particular, dryout is a common problem in two-phase microchannel heat sinks used for electronic cooling. The formation of sufficiently large bubbles that block the channels leads to the diversion of the fluid into other channels which greatly reduces heat removal in the blocked channels [5, 7, 8].

Some of the methods suggested for facilitating bubble removal in microchannels include the use of T-shaped non clogging microchannels [9], tapered structures [1], hydrophilic-hydrophobic patterning [10], and hydrophobic porous membranes [11, 12].

Most of the previous studies attributed the lack of motion of stagnant bubbles to resistant capillary forces related to pressure differences across the front and back interfaces [2, 13-17]. Herein we investigate pinning forces along *triple* contact lines as another factor hindering the

motion of dry bubbles. Note that lubricated bubbles have no triple contact line and do not experience pinning.

To the best of authors' knowledge, the only studies to account for the pinning forces acting on a bubble in the force balance are studies by Blackmore et al. [18] and Metz et al. [1]. Blackmore et al. [18] modeled the forces acting on a small stagnant bubble confined between two parallel plates at the moment of detachment. Their model included viscous drag and pinning forces but overlooked capillary forces. The pinning force was derived as an integration of the projection of surface tension on the solid surface plane over the bubble's contact perimeter. Metz et al. [1] modeled the forces acting on a moving bubble in a microchannel as the superposition of the capillary force, viscous drag, and the drag induced due to thin film deposition, pinning, and contact angle dynamics. Their simple model for the pinning forces linearly correlates this force to a constant pinning coefficient, the length of the gas bubble contact line, and the surface tension. For their experiments, the pinning coefficient and subsequently the pinning force turned out to be negligible which was attributed to the high surface quality of the glass channels and the disappearance of contact lines in lubricated bubbles.

Because of *dewetting*, elongated bubbles moving in microfluidic systems are not always lubricated. Dewetting refers to the spontaneous withdrawal of a liquid film from a partially wetting surface [19]. On a totally wetting substrate, a film is always stable while on a partially wetting surface, thin films below a critical thickness are metastable and may dewet by nucleation and the growth of a dry zone. The critical thickness for an ideal surface is given by

$$e_{crit} = 2\kappa^{-1} \sin\left(\theta_{equ} / 2\right) \tag{1}$$

where κ^{-1} is the capillary length defined by $\sqrt{\sigma / \rho g}$ [19]. Non-ideal surfaces which are marred by chemical or physical surface irregularities exhibit contact angle hysteresis. For those surfaces, θ_{equ} must be replaced with θ_{rec} in Eq. (1).

The nucleation of a dry zone may start with a local surface defect or by a perturbation; the zone expands if its radius exceeds a critical value. For an air-water system with a receding contact angle as low as 1°, the critical thickness becomes about $45\ \mu m$, much thicker than a possible liquid film around an elongated bubble in microchannels. Because microfluidic systems are not usually free of surface defects, the chances for dewetting of the thin films around bubbles are relatively high. The dewetting velocity with which the dry zone opens up is constant,

$$U_{dew} = \frac{k\sigma}{\mu}\theta_{rec}^{3} \tag{2}$$

where k is an empirical coefficient that depends on the nature and molecular weight of the fluid and also the solid surface quality [20].

The existence of lubricating films around bubbles in a partially wetting microchannel depends on the bubble velocity, the dewetting velocity, the length of the bubbles, and the microchannel cross-sectional dimensions [21]. Experimental results from Cubaud and Ho [21] have shown that, in a partially wetting square channel, bubbles moving slower than the dewetting velocity are completely dry. For velocities between the dewetting velocity and a critical velocity, the rear of the bubble is dried out while the front of the bubble remains lubricated (hybrid bubbles). At velocities higher than the critical velocity, bubbles are lubricated. The critical velocity was estimated by

$$U_{crit} \approx U_{dew} l_b / h \tag{3}$$

where l_b is the length of the bubble and h is the width of the square microchannel [21]. Further experimental data is required to develop such a correlation for rectangular channels. Figure 1 presents images of dry, hybrid, and lubricated bubbles. The presence of droplets on the channel walls around a bubble is indicative of dewetting.

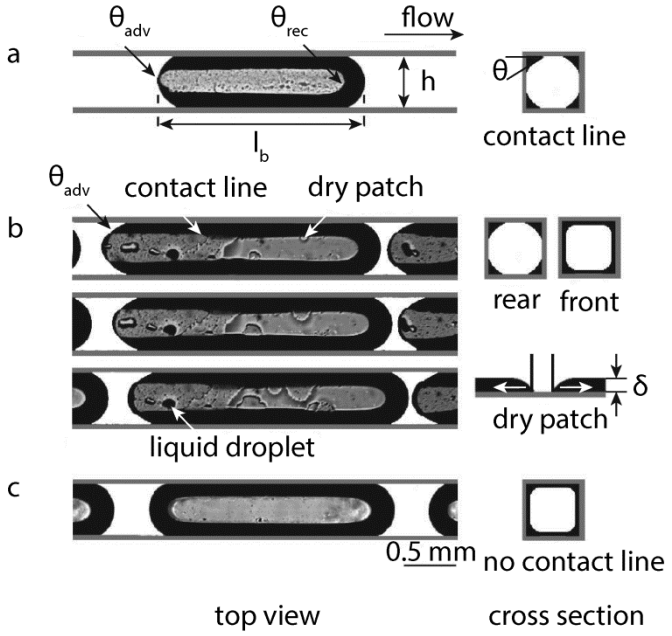

Figure 1: Bubbles with different wetting conditions: a) dry bubble, b) consecutive images of a hybrid bubble, and c) lubricated bubble, adapted from Cubaud and Ho [21]

We reviewed the conditions leading to the presence of dry bubble in microchannels. Because of the contact angle hysteresis on a non-ideal surface, a dry moving bubble forms different dynamic contact angles at the front and back. The pinning forces applied on the contact lines and the possible capillary pressure induced by pinning resist the motion of a dry bubble. At low flow velocities, the pressure difference across the length of the bubble may not be enough to overcome these forces. In such a situation, the bubble becomes stationary. If there is no bypass

for the flow, the bubble eventually starts crawling due to the liquid accumulation and pressure buildup behind it. When a bypass (e.g. a parallel channel or corner flow) exists, the bubble may remain stationary indefinitely and an increase of flow rate would be required to move the bubble forward [18]. Dry stationary bubbles present in our microchannel array device, as shown in Figure 2, further motivate this theoretical and experimental study of the pressure required to stimulate motion of dry bubbles and effectively clear the channel.

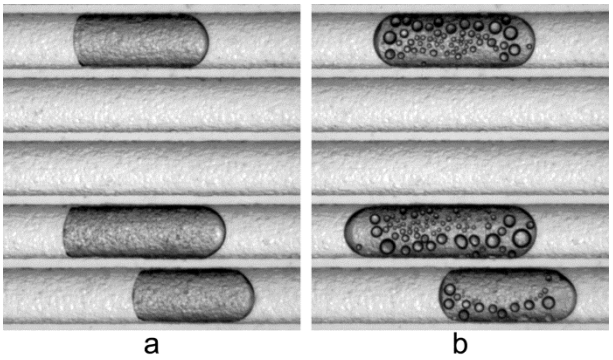

Figure 2: Dry stationary bubbles in a polycarbonate microchannel array where clear channels act as a bypass for the flow. Upon stagnation small droplets start to condense and grow on the channel walls inside the saturated bubbles. a and b were taken upon stagnation and 17 minutes after, respectively.

2 Theoretical model

In this section a theoretical model that describes the roles of contact line forces on the bubble pinning phenomenon is proposed. de Gennes et al. [19] have described the forces acting on a *dynamic* triple contact line on non-ideal surfaces. Herein, we develop the force balance equations for the situation where an external force on the contact line is not enough to initiate movement. Then we expand our model for a clogging bubble having two contact lines at its front and back.

Young's equation presents the balance of forces for a triple contact line at equilibrium as

$$\sigma_{lg}\cos\theta_{equ} = \sigma_{sg} - \sigma_{sl} \tag{4}$$

When an external force is applied on a contact line, the contact angle varies from the local equilibrium contact angle. For the liquid segment in the circular tube described in Figure 3 the force equilibrium yields

$$F = s(\sigma_{sg} - \sigma_{sl} - \sigma_{lg}\cos\theta) \tag{5}$$

where s refers to the arc length of the contact line. The magnitude of this force is equal to the magnitude of the pinning force which acts in the opposite direction and resists motion. Substituting the term $\sigma_{sg} - \sigma_{sl}$ from Young's equation we get

$$F = s\sigma_{lg}(\cos\theta_{equ} - \cos\theta) \tag{6}$$

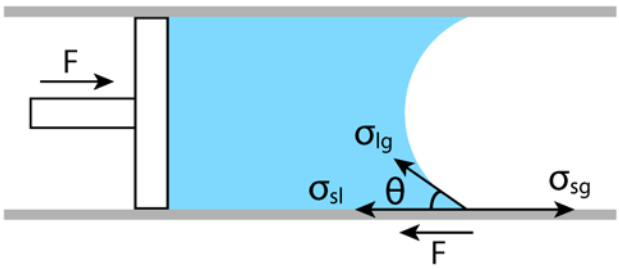

Figure 3: Pinning forces resisting motion under the action of a piston in a circular tube, adapted from de Gennes et al. [19]

Similar forces acts on the back and front (left and right) *triple* contact lines (s_L and s_R) of a clogging bubble in a rectangular channel as shown in Figure 4a.

$$F_L = s_L\sigma_{lg}(\cos\theta_{equ} - \cos\theta_L) \tag{7}$$

$$F_R = s_R\sigma_{lg}(\cos\theta_R - \cos\theta_{equ}) \tag{8}$$

Depending on the hydrophilicity and geometry of the channel liquid regions may or may not be present in the corners of the channel, as illustrated in Figure 4b and Figure 4c. Liquids with

equilibrium contact angles below 45° most likely occupy the corner regions in rectangular channels [22].

In the presence of corner liquid regions, we can assume slip boundary conditions on the gas-liquid interface since $\mu_g << \mu_l$ and the velocity gradient inside the bubble is small. We also know that for $Ca << 1$, viscous forces are negligible compared to capillary forces. Therefore, we can assume the effect of drag forces exerted by the corner flow on the bubble is negligible.

The contact angle of the non-ideal surface varies between the receding and advancing contact angles. The maximum external force that can be compensated by pinning corresponds to the situation where the contact angle equals the advancing or the receding contact angle, depending on the direction of the force. Therefore, for the continuous motion of the contact line the external forces must be larger than the maximum pinning forces.

$$F_L \geq s_L \sigma_{lg} (\cos\theta_{equ} - \cos\theta_{adv}) \tag{9}$$

$$F_R \geq s_R \sigma_{lg} (\cos\theta_{rec} - \cos\theta_{equ}) \tag{10}$$

The external forces on the bubble are the result of the pressure field maintained by the corner flows. These forces can be approximated by

$$F_L = A_L (P_L - P_g) \tag{11}$$

$$F_R = A_R (P_g - P_R) \tag{12}$$

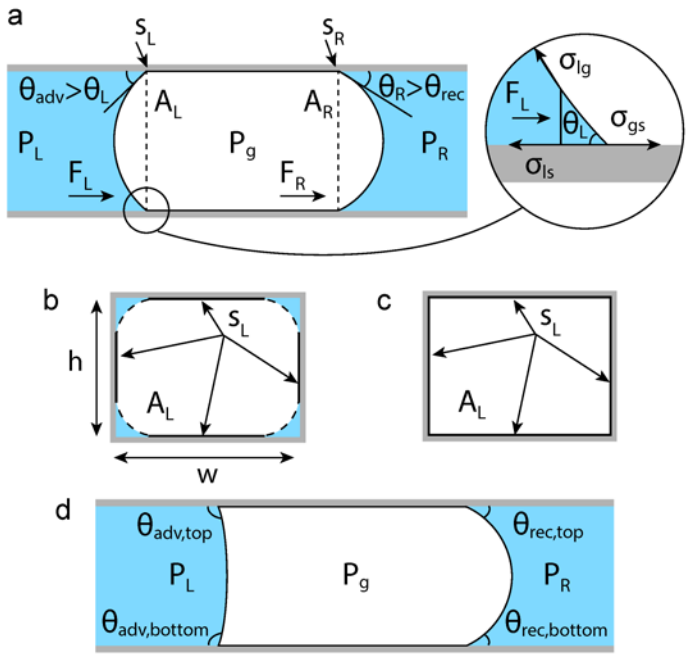

Figure 4: a) Side view of a stationary bubble and forces applied on it by the pressure field and the channel walls, b and c) channel cross section at the left contact line with and without liquid in the corner regions, respectively, note that the dotted border is not a part of the triple contact line but rather a gas liquid interface, d) a moving bubble with a convex back interface

where A_L and A_R are the bubble cross sectional areas at the back and front, respectively. These are slightly different from the microchannel cross sectional area when bubbles do not occupy the corner regions [23].

In order for a bubble with a concave interface on the back $(\theta_{adv} < 90^\circ)$ to move Eq. (9) and (10) should both be satisfied. By substituting Eqs. (11) and (12) into Eq. (9) and (10) we get

$$P_L - P_g \geq \frac{s_L}{A_L}\sigma_{lg}(\cos\theta_{equ} - \cos\theta_{adv}) \tag{13}$$

$$P_g - P_R \geq \frac{s_R}{A_R}\sigma_{lg}(\cos\theta_{rec} - \cos\theta_{equ}) \tag{14}$$

Assuming that the bubble has equal cross sectional areas, contact line lengths, and equilibrium contact angles at the front and the back, adding Eq. (13) to Eq. (14) yields

$$P_L - P_R \geq \frac{s}{A}\sigma_{lg}(\cos\theta_{rec} - \cos\theta_{adv}) \tag{15}$$

For a square channel with a width of h, Eq. (15) simplifies to

$$P_L - P_R \geq 4\sigma_{lg}\frac{(\cos\theta_{rec} - \cos\theta_{adv})}{h} \tag{16}$$

Considering only the pinning forces, Eq. (16) provides the necessary condition for bubble motion for θ_{rec} and $\theta_{adv} < 90^{\circ}$. However, it is not a sufficient condition for movement as both Eqs. (13) and (14) should be simultaneously satisfied.

For a bubble with a convex interface on the back $(\theta_{adv} > 90^{\circ})$, as shown in Figure 4d, the required condition for motion of the back interface might be different. Pinning forces cannot effectively contribute to the force balance written for a fluid element at the bulged interface. If the pressure difference across the interface exceeds what interfacial forces can compensate for according to the Young-Laplace equation, the interface will break up and move forward. In this case

$$P_L \geq P_g - 4\sigma_{lg}\frac{\cos\theta_{adv}}{h} \tag{17}$$

This condition is met before the pinning forces are overcome. Capillary valves often work based on this principle [11, 24, 25]. Note that at the front interface, pressure differences up to $4\sigma\cos\theta_{equ}/h$ can be easily held by surface tension. However, for higher pressure differences and subsequently front contact angles below θ_{equ}, the pinning forces are responsible for the

integrity of the interface. The motion of the front interface is always triggered by overcoming the pinning forces.

Adding Eq. (17) and Eq. (14) written for a square microchannel results in the necessary condition for the motion of both the front and the back contact lines

$$P_L - P_R \geq 4\sigma_{lg} \frac{(\cos\theta_{rec} - \cos\theta_{equ} - \cos\theta_{adv})}{h} \tag{18}$$

Therefore, our theoretical model consists of two parts: Eq. (16) for concave back bubbles and Eq. (18) for convex back bubbles with some exceptions. Our experimental results suggest that for moving bubbles with a slightly bulged back interface $(90^\circ \leq \theta_{adv} \leq 93^\circ)$, Eq. (16) can predict the pressure difference across the bubble much better than Eq. (18). For slightly bulged interfaces, the pinning forces may be still able to assist the surface tension to withstand the pressure difference across the meniscus and the motion of the back contact line happens by overcoming the pinning forces.

It is important to note that in the absence of liquid regions in the corners of the channel, pinning forces are the only resistive forces acting on the bubbles. Moreover, the length of the bubble does not influence the pressure difference across the bubble. However, when liquid regions exist, capillary forces may act on the bubble as well [13, 26] and the pressure drop across the bubble becomes a function of the bubble length.

2.1 Differentiation between capillary and pinning forces

It is easy to confuse capillary and pinning forces because the mathematical form of the right hand of Eq. (15) looks similar to capillary pressure if we replace s and A with $2\,(w+h)$ and $w \times h$, respectively. It is important to distinguish between the concepts of capillary and pinning forces

and to understand that both of these forces may act on a dry bubble. In our example, the capillary pressure gradient was caused by the difference in the back and front curvatures due to pinning and contact angle hysteresis. An integration of capillary pressure over the interface results in the capillary force [1].

It is also possible to have capillary forces in the absence of pinning; for example, lubricated bubbles passing through contractions or expansions experience capillary forces [1]. The capillary pressure gradient and subsequently the capillary force can also be produced by a surface tension gradient due to variations in the temperature, concentration, or electric field [22].

Unlike pinning forces which always resist the motion, capillary forces may stimulate it. An interesting example presented by Paust et al. [27] demonstrates a conflict between the capillary and pinning forces: A growing bubble in a tapered geometry is pinned at the back side. The bubble growth toward a bigger cross section reduces the front curvature and increases the capillary force which eventually overcomes the pinning force at the back and detaches the bubble from the pinning point.

2.2 Capillary Pressure

In the presence of liquid regions in the corner of a channel, the capillary pressure gradient induces an interfacial liquid flow on the gas-liquid menisci (represented by dotted line in Figure 4b) from the back to front that wants to move the bubble backward [22, 27]. Indeed, the corner liquids act as a medium for implementing the capillary pressure. The maximum capillary pressure gradient occurs when both front and back contact angles hold their limiting values. For a rectangular channel with a width of w and depth of h the Young-Laplace equation yields

$$\Delta P_{cap} = 2\sigma_{lg}\left(\cos\theta_{rec} - \cos\theta_{adv}\right)\left(\frac{1}{w} + \frac{1}{h}\right) \tag{19}$$

The possibility of the capillary pressure to be completely transferred through the small gas-liquid menisci is an open question. If it does ΔP_{cap} should be added to the right hand side of Eq. (15) to result in the necessary condition for the onset of bubble motion

$$P_L - P_R \geq \sigma_{lg}(\cos\theta_{rec} - \cos\theta_{adv})\left[\frac{s}{A} + 2\left(\frac{1}{w} + \frac{1}{h}\right)\right] \tag{20}$$

The pressure drop along the length of the bubble is maintained by the bypassing corner flow. Treating the corner flow as Poiseuille flow, Wong et al. [13] approximated the pressure drop along a stationary bubble by

$$P_L - P_R = \frac{128Q\mu l_b}{\pi d_{eff}^4} \tag{21}$$

where Q is the volumetric flow rate and d_{eff} is the effective dynamic diameter of the liquid flow. Longer bubbles apply more resistant to the corner flow and experience a larger pressure difference across their length. Equation (21) suggests that for any bubble length there is a critical flow rate that provides a pressure drop sufficient for bubble motion. The dynamic contact angles of the front and back of the dry moving bubble vary between receding and advancing contact angles as the triple contact line still exists. If the velocity of a dry bubble becomes high enough a thin film around the bubble will start to form and eventually the bubble will become lubricated again [28], as shown in Figure 5. As the velocity increases the bubble caps deform asymmetrically resulting in the so-called “bullet-shaped” appearance [22, 29].

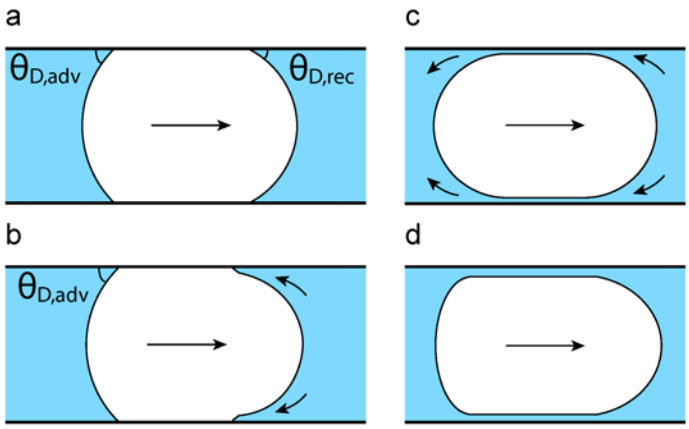

Figure 5: Progression of bubble shape with increasing velocity: a) dry dynamic bubble, b) thin film forming, c) lubricated bubble, and d) bullet-shaped lubricated bubble, adapted from Jensen [28]

3 Theoretical model validation

The objective of the experiments is to measure the pressure required behind a dry bubble (with no corner flow and hence no resistive capillary pressure) to overcome the pinning forces and maintain its crawling motion in a square channel. At low velocities $(\mathrm{Re} << 1)$, inertial forces are negligible and we can assume that the pinning forces are the only forces resisting the motion. Furthermore, at low velocities $(Ca < 10^{-3})$, dynamic contact angles are independent of velocity and are equal to the static receding and advancing contact angles [30]. Equations (16) and (18) will be validated for bubbles with concave or convex back interfaces, respectively.

3.1 Experimental setup and procedure

A schematic view of the experimental setup is presented in Figure 6. Square borosilicate glass channels (VitroCom PN 8100) with a height and width of 976 ± 8 μm and a length of 10 cm have been used as the test channels. In order to decrease the hydrophilicity of the glass and have contact angle readings with high accuracy, four brand new channels were washed with "Rain X

Original" glass treatment solution for $1-3$ seconds and then rinsed with water and dried with compressed air. Depending on the duration of the treatment and the velocity of solution injection, each glass channel show different receding and advancing contact angles in the experiments. The fluid used in the experiments was deionized water. The treatment increased the equilibrium contact angle of water on the channel surface from below 10° to $60^{\circ}-85^{\circ}$.

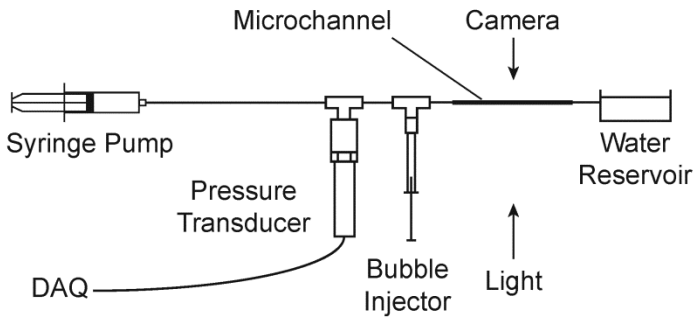

Figure 6: Experimental setup for pressure measurements

A syringe pump (Harvard Apparatus PHD 2000 Programmable) was used for flow delivery. A 100-μl gastight syringe (Hamilton PN 81020) was used for bubble injection. The imaging system consisted of a LaVision sCMOS camera coupled with a Navitar 12X Zoom lens. An incandescent 100-Watt globe lamp was used for backlighting.

A pressure transducer (Omega PX409-10WG5V) with a range of $0-2490$ Pa and a 0.08% accuracy $(\pm 2$ Pa) was used for pressure measurement. The pressure signal was recorded with an NI-USB 6211 DAQ system and LabVIEW. Several precautions were taken to reduce the pressure fluctuations in the room and test loop including limiting changes in the lab environment. The pressure transducer was connected to its fittings under water to avoid air trapping in the fittings and the transducer branch.

The flow rate was set at $2\ \mu l/min$ which corresponds to an average velocity of 2 mm/min in the channels $(Ca < 10^{-6})$. A single bubble with a volume between 5 to 10 μl was injected into the flow stream for each experiment. To verify the repeatability, on two of the channels, two sets of experiments were performed.

The required pressure to maintain a flow rate of $2\ \mu l/min$ was measured prior to bubble injection. The periodically averaged pressure values for every 0.2 s interval prior to bubble injection were relatively steady and the variations were within the ± 2 Pa accuracy range of the transducer. The change in the water reservoir level between this reading and the beginning of image and pressure acquisition is carefully calculated for each experiment $(< 120\ \mu m)$ and accounted for. We are interested in the pressure difference across the bubble length; therefore, the pressure prior to bubble injection was subtracted from the measured pressure during bubble motion. The change in the reservoir water level during image and pressure acquisition was about $29\ \mu m$ (0.28 Pa hydrostatic pressure) and was neglected.

Image and pressure data acquisition started almost simultaneously at rates of 5 fps and 1000 Hz respectively and continued for 12 minutes. The pressure data has been condensed to an average pressure value for every 0.2 s interval. By matching a pressure peak in the pressure signal to its corresponding closely-timed image with an apparent maximum pinning, the lag between the imaging and pressure measurements was revealed. Using this information, each image has been mapped to a single pressure reading.

3.2 Results

In order to calculate the required pressure to keep the bubbles moving from Eq. (16) and Eq. (18) the contact angles must be measured from the images. Accurate measurement of the contact angles is only possible when the image of the bubble interface is a uniform line as shown in Figure 7a and Figure 7c, in contrast to Figure 7b and Figure 7d. For the selected images, accurate measurement of the contact angles was possible. Furthermore, within one second before and after the image was captured the motion of the bubble was steady and there was no observed rapid change in the shape of the front and back interfaces. For those cases, the variation in the measured pressure during the two second period was always within and often much lower than ± 2 Pa accuracy range of the transducer.

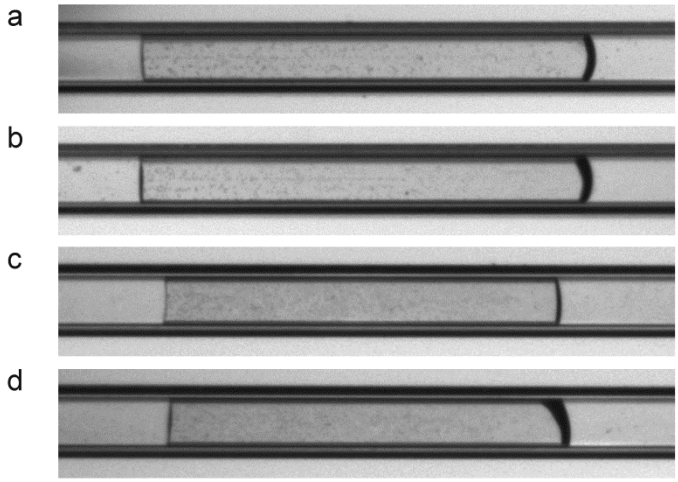

Figure 7: Variation in the contact angles during the motion, a and b are images of one bubble and c and d are images of another. a) concave back interface, c) convex back interface, b and d) nearly flat back interfaces and unequal front contact angles at the side walls

The top and bottom contact angles of an interface (see Figure 4d) are often different and the average of their cosine values should be used instead in the equations. To use Eq. (18) the equilibrium contact angle must be known. We have estimated the cosine of the equilibrium contact angle by averaging the cosine of the advancing and receding contact angles of all the

selected occurrences in each dataset [31, 32]. In reality, the equilibrium contact angle varies locally but we have assumed it to be a single value in each data set.

Table 1 presents the length of the bubbles in each experiment and the range of the advancing and receding contact angles for the selected occurrences. It is possible to either have a concave or a convex back interface when one of the back contact angles (top or bottom contact angles) is below 90° and the other one is above 90°.

Table 1: Details of the six sets of experiments

Experiment No.	Channel No.	Length of the injected bubble (mm)	θ_{rec}(deg) of occurrences	θ_{adv}(deg) of occurrences
1	1	8.1	70 – 83	87 – 97
2	1	10.2	69 – 84	86 – 94
3	2	9.3	56 – 70	77 – 90
4	3	5.3	44 – 60	93 – 98
5	4	5.6	68 – 81	89 – 97
6	4	5.4	66 – 78	86 – 96

Figure 8 presents a sample measured pressure difference across the bubble length over time. The values of receding and advancing contact angles vary locally and the peak pressure values correspond to severe pinning cases.

Figure 9 presents an overview of the measured pressures in the six sets of experiments and the model's predictions. For bubbles with a concave back interface, the convex back model underestimates the required pressure to move the bubbles while for bubbles with a convex back interface, the concave back model overestimates the required pressure.

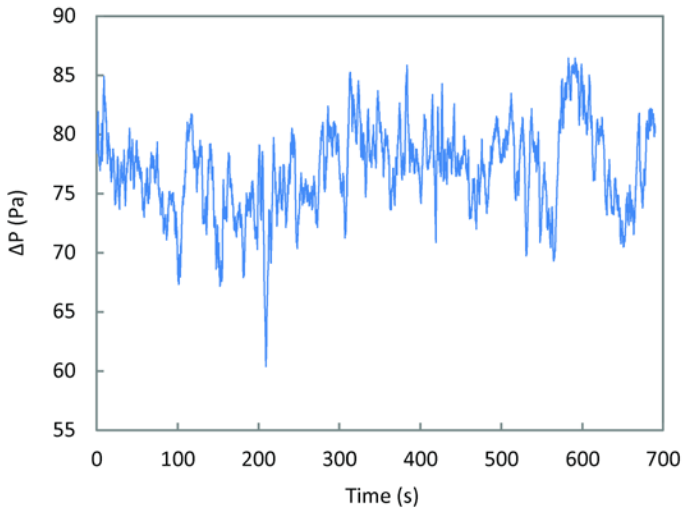

Figure 8: Variation in pressure difference across the length of a crawling bubble over time which is due to pinning and variation in the local surface conditions and contact angles

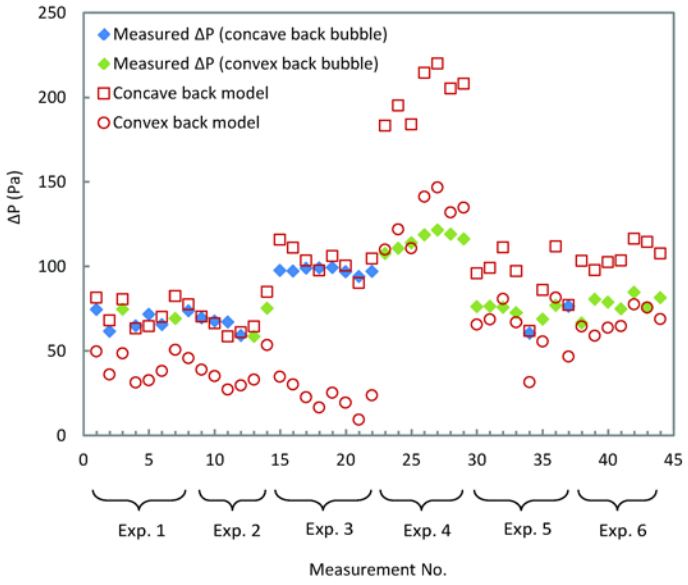

Figure 9: Comparison between the model's predictions and the measured pressures for the 6 sets of experiments. There could be a large difference between the concave and convex back model predictions.

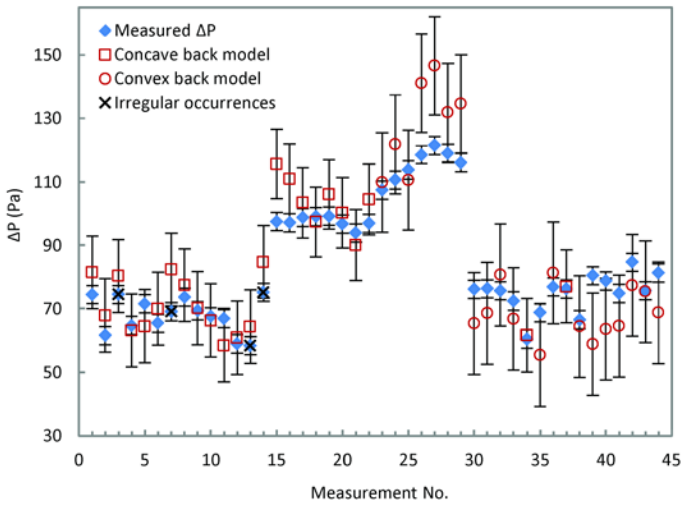

Figure 10: Comparison between the measured pressure and the matching models' prediction. There are four irregular occurrences that have a slightly convex back interface but match the concave back model's prediction better.

The measured pressure is compared with the model's predictions for bubbles in the six sets of experiments in Figure 10. Four of the occurrences have advancing contact angles slightly larger than 90° ($90^{\circ} \le \theta_{adv} \le 93^{\circ}$) but they matched the concave back model's prediction better. We presume for those four consequences the motion of the back contact line was achieved by overcoming pinning forces and not by failure of the meniscus in withstanding the pressure difference across it. Figure 11 gives an overview of the normalized model's predictions with respect to measured pressures. The model successfully predicts the required pressure to maintain the crawling motion of the bubbles.

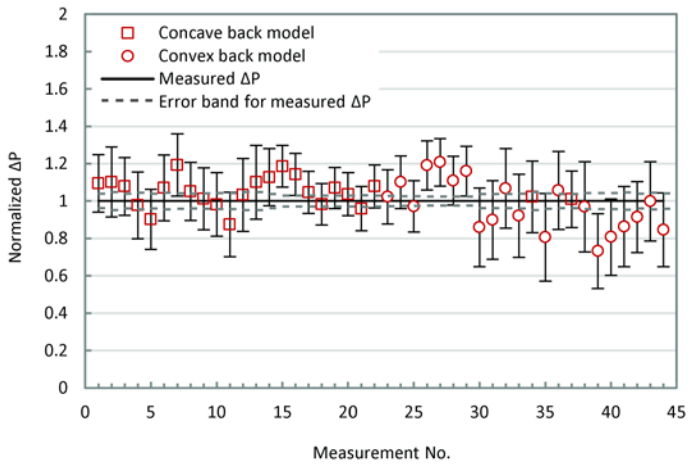

Figure 11: Normalized models' predictions based on the measured pressure

The errors were calculated using the Kline and McClintock method [33]. The quantified errors associated with pressure measurements prior to bubble injection and during bubble motion are due to the accuracy limits of the transducer $(\pm 2\ \text{Pa})$. The variations of the periodically averaged pressure values prior to bubble injection were within the accuracy range. Therefore, pressure fluctuations sourced from the syringe pump or room pressure were not quantifiable and have been neglected in error estimations.

The errors associated with the concave model's prediction include uncertainty in the size of the channel $(\pm 8\ \mu\text{m})$ and uncertainty in the measurement of the four contact angles for a bubble due to image resolution and thresholding $(\pm 2.25^{\circ})$. An additional error is involved in the prediction of convex back model due to the estimation of the equilibrium contact angle which results in larger error bars for the convex back model's predictions. The cosine of equilibrium contact angle was estimated by averaging the cosine of advancing and receding contact angles of studied occurrences in each data set. A standard error of $\pm 2.25^{\circ}$, equal to the uncertainty in contact angle measurements, was *assigned* to this estimation of the equilibrium contact angle.

One of the most important factors contributing to the differences observed between the measured pressure and the model's predictions is the contact angle measurement. With a two dimensional image from the bubble caps it is not possible to measure the contact angles on all 4 sides of the channel. We only measure the contact angles on the top and bottom sides of the bubble caps (as shown in Figure 4d). We assume that the cosine of contact angles on the other two sides are an average of the cosine of contact angles on the top and bottom sides. For a uniform cap this assumption is reasonable but may not be accurate. Some assumptions were made in the development of our theoretical model such as assuming equal cross sectional areas, contact line lengths, and equilibrium contact angles at the front and the back of the bubbles. There is a definite deviation from these assumptions in the experiments which also contributes to the differences between the measured pressure and the model's predictions. For example in the development of the model, Eq. (15) was derived by adding Eq. (13) and (14). If it turns out that $s_L / A_L = 0.99\, s_R / A_R = 0.99(4/h)$ the model prediction by Eq. (16) will overestimate the required pressure by $0.04\sigma_{lg}(\cos\theta_{equ} - \cos\theta_{adv})/h$.

4 Conclusions

A bipartite theoretical model that describes the required pressure to initiate the motion of a dry bubble in a partially hydrophilic channel is proposed. It has been shown that the motion of the front interface of the bubble always occur by overcoming pinning forces. However, the motion of the back interface may occur either by overcoming the pinning forces or by failure of the meniscus in withstanding the pressure difference across it. The theoretical model has been validated by experimental results. This work differentiates the resistive pinning forces from the

capillary pressure which may get transmitted by the gas-liquid interface in the presence of corner flow.

The use of highly hydrophilic surfaces is an effective solution for reducing bubble clogging at low velocities. At small equilibrium contact angles, $\cos\theta_{rec} - \cos\theta_{adv}$ is essentially smaller than the one for large equilibrium contact angles even with similar hysteresis. Therefore, dry bubbles experience smaller pinning and capillary forces resisting their motion. Surfaces with smaller receding contact angles also exhibit a lower dewetting velocity and the bubbles will have a better chance of remaining lubricated at low flow rates.

Acknowledgement

This work has been supported by National Institutes of Health (NIH) Contract No. 1 R01 EB011567-01A1.

Nomenclature

A	Cross sectional area of bubble
d_{eff}	Effective dynamic diameter of the corner flow
F	Force
P	Pressure
Q	Flow rate
U	Velocity
e	Thickness
g	Gravitational acceleration
h	Microchannel height
k	Dewetting coefficient
l	Length
s	Length of the contact line
w	Microchannel width

Greek symbols

θ	Contact angle
κ^{-1}	Capillary length $\kappa^{-1} = \sqrt{\sigma / \rho g}$
ρ	Density
μ	dynamic viscosity
σ, σ_{lg}	Liquid-gas surface tension
σ_{sg}	Gas-solid surface free energy
σ_{sl}	Liquid-solid surface free energy

Subscripts

D	Dynamic
L	Left
R	Right
adv	Advancing
b	Bubble
cap	Capillary
$crit$	Critical
dew	Dewetting
equ	Equilibrium
g	Gas
rec	Receding

References

[1] Metz, T., Paust, N., Zengerle, R., and Koltay, P., 2010, "Capillary Driven Movement of Gas Bubbles in Tapered Structures," Microfluid Nanofluid, 9(2-3), pp. 341-355.

[2] Kohnle, J., Waibel, G., Cernosa, R., Storz, M., Ernst, H., Sandmaier, H., Strobelt, T., and Zengerle, R., "*A Unique Solution for Preventing Clogging of Flow Channels by Gas Bubbles*," Proc. 15th IEEE International Conference on Micro Electro Mechanical Systems, IEEE MEMS, pp. 77-80.

[3] Litterst, C., Eccarius, S., Hebling, C., Zengerle, R., and Koltay, P., 2006, "Increasing μDMFC Efficiency by Passive CO2 Bubble Removal and Discontinuous Operation," Journal of Micromechanics and Microengineering, 16(9), pp. S248-S253.

[4] Kandlikar, S., and Balasubramanian, P., 2003, "*Effect of Channel Shape on Flow Pattern During Flow Boiling in Single and Parallel Rectangular Microchannels*," Proc. 5th International Conference on Boiling Heat Transfer, Montego Bay, Jamaica.

[5] Kenny, T. W., Goodson, K. E., Santiago, J. G., Wang, E., Koo, J.-M. O., Jiang, L., Pop, E., Sinha, S., Zhang, L., Fogg, D., Yao, S., Flynn, R., Chang, C.-H., and Hidrovo, C. H., 2006, "Advanced Cooling Technologies for Microprocessors," International Journal of High Speed Electronics and Systems, 16, pp. 301-313.

[6] Kuo, C. Y., and Pan, C., 2009, "The Effect of Cross-Section Design of Rectangular Microchannels on Convective Steam Condensation," Journal of Micromechanics and Microengineering, 19(3), p. 035017.

[7] Chen, T., and Garimella, S. V., 2011, "A Study of Critical Heat Flux During Flow Boiling in Microchannel Heat Sinks," Journal of Heat Transfer, 134(1), pp. 011504-011504.

[8] Mukherjee, S., and Mudawar, I., 2003, "Smart Pumpless Loop for Micro-Channel Electronic Cooling Using Flat and Enhanced Surfaces," IEEE Transactions on Components and Packaging Technologies, 26(1), pp. 99-109.

[9] Litterst, C., Metz, T., Zengerle, R., and Koltay, P., 2008, "Static and Dynamic Behaviour of Gas Bubbles in T-Shaped Non-Clogging Micro-Channels," Microfluid Nanofluid, 5(6), pp. 775-784.

[10] Hibara, A., Iwayama, S., Matsuoka, S., Ueno, M., Kikutani, Y., Tokeshi, M., and Kitamori, T., 2004, "Surface Modification Method of Microchannels for Gas−Liquid Two-Phase Flow in Microchips," Analytical Chemistry, 77(3), pp. 943-947.

[11] Zhu, X., 2009, "Micro/Nanoporous Membrane Based Gas–Water Separation in Microchannel," Microsystem Technologies, 15(9), pp. 1459-1465.

[12] Xu, J., Vaillant, R., and Attinger, D., 2010, "Use of a Porous Membrane for Gas Bubble Removal in Microfluidic Channels: Physical Mechanisms and Design Criteria," Microfluid Nanofluid, 9(4-5), pp. 765-772.

[13] Wong, C. W., Zhao, T. S., Ye, Q., and Liu, J. G., 2005, "Transient Capillary Blocking in the Flow Field of a Micro-DMFC and Its Effect on Cell Performance," Journal of The Electrochemical Society, 152(8), p. A1600.

[14] Rapolu, P., and Son, S. Y., 2011, "Characterization of Wettability Effects on Pressure Drop of Two-Phase Flow in Microchannel," Experiments in Fluids, 51(4), pp. 1101-1108.

[15] Paust, N., Krumbholz, S., Munt, S., Müller, C., Koltay, P., Zengerle, R., and Ziegler, C., 2009, "Self-Regulating Passive Fuel Supply for Small Direct Methanol Fuel Cells Operating in All Orientations," Journal of Power Sources, 192(2), pp. 442-450.

[16] Gravesen, P., Branebjerg, J., and Jensen, O. S., 1993, "Microfluidics-a Review," Journal of Micromechanics and Microengineering, 3, pp. 168-182.

[17] Hutzenlaub, T., Paust, N., Zengerle, R., and Ziegler, C., 2011, "The Effect of Wetting Properties on Bubble Dynamics and Fuel Distribution in the Flow Field of Direct Methanol Fuel Cells," Journal of Power Sources, 196(19), pp. 8048-8056.

[18] Blackmore, B., Li, D., and Gao, J., 2001, "Detachment of Bubbles in Slit Microchannels by Shearing Flow," Journal of Colloid and Interface Science, 241(2), pp. 514-520.

[19] de Gennes, P. G., Brochard-Wyart, F., and Quéré, D., 2004, *Capillarity and Wetting Phenomena : Drops, Bubbles, Pearls, Waves*, Springer, New York, pp. 37, 153-174.

[20] Redon, C., Brochard-Wyart, F., and Rondelez, F., 1991, "Dynamics of Dewetting," Physical Review Letters, 66(6), pp. 715-718.

[21] Cubaud, T., and Ho, C. M., 2004, "Transport of Bubbles in Square Microchannels," Physics of Fluids, 16(12), pp. 4575-4585.

[22] Ajaev, V. S., and Homsy, G. M., 2005, "Modeling Shapes and Dynamics of Confined Bubbles," Annual Review of Fluid Mechanics, 38(1), pp. 277-307.

[23] Wong, H., Morris, S., and Radke, C. J., 1992, "Three-Dimensional Menisci in Polygonal Capillaries," Journal of Colloid and Interface Science, 148(2), pp. 317-336.

[24] Berthier, J., Loe-Mie, F., Tran, V. M., Schoumacker, S., Mittler, F., Marchand, G., and Sarrut, N., 2009, "On the Pinning of Interfaces on Micropillar Edges," Journal of Colloid and Interface Science, 338(1), pp. 296-303.

[25] Cho, H., Kim, H. Y., Kang, J. Y., and Kim, T. S., 2007, "How the Capillary Burst Microvalve Works," Journal of Colloid and Interface Science, 306(2), pp. 379-385.

[26] Jensen, M. J., Goranovi, G., and Bruus, H., 2004, "The Clogging Pressure of Bubbles in Hydrophilic Microchannel Contractions," Journal of Micromechanics and Microengineering, 14(7), pp. 876-883.

[27] Paust, N., Litterst, C., Metz, T., Eck, M., Ziegler, C., Zengerle, R., and Koltay, P., 2009, "Capillary-Driven Pumping for Passive Degassing and Fuel Supply in Direct Methanol Fuel Cells," Microfluid Nanofluid, 7(4), pp. 531-543.

[28] Jensen, M. J., 2002, "Bubbles in Microchannels. Dissertation," Master of Science, Technical University of Denmark, Lyngby.

[29] Chang, H.-C., 2001, "*Bubble/Drop Transport in Microchannels*," The MEMS Handbook, CRC Press.

[30] Kim, H.-Y., Lee, H. J., and Kang, B. H., 2002, "Sliding of Liquid Drops Down an Inclined Solid Surface," Journal of Colloid and Interface Science, 247(2), pp. 372-380.

[31] Miyama, M., Yang, Y., Yasuda, T., Okuno, T., and Yasuda, H. K., 1997, "Static and Dynamic Contact Angles of Water on Polymeric Surfaces," Langmuir, 13(20), pp. 5494-5503.

[32] Della Volpe, C., Maniglio, D., Siboni, S., and Morra, M., 2001, "An Experimental Procedure to Obtain the Equilibrium Contact Angle from the Wilhelmy Method," Oil & Gas Science and Technology Rev IFP, 56(1), pp. 9-22.

[33] Kline, S. J., and McClintock, F. A., 1953, "Describing Uncertainties in Single-Sample Experiments," Mechanical Engineering, 75, pp. 3-8.

List of Table Captions

List of Figure Captions

Figure 1: Bubbles with different wetting conditions: a) dry bubble, b) consecutive images of a hybrid bubble, and c) lubricated bubble, adapted from Cubaud and Ho [21]

Figure 2: Dry stationary bubbles in a polycarbonate microchannel array where clear channels act as a bypass for the flow. Upon stagnation small droplets start to condense and grow on the channel walls inside the saturated bubbles. a and b were taken upon stagnation and 17 minutes after, respectively.

Figure 3: Pinning forces resisting motion under the action of a piston in a circular tube, adapted from de Gennes et al. [19]

Figure 4: a) Side view of a stationary bubble and forces applied on it by the pressure field and the channel walls, b and c) channel cross section at the left contact line with and without liquid in the corner regions, respectively, note that the dotted border is not a part of the triple contact line but rather a gas liquid interface, d) a moving bubble with a convex back interface

Figure 5: Progression of bubble shape with increasing velocity: a) dry dynamic bubble, b) thin film forming, c) lubricated bubble, and d) bullet-shaped lubricated bubble, adapted from Jensen [28]

Figure 6: Experimental setup for pressure measurements

Figure 7: Variation in the contact angles during the motion, a and b are images of one bubble and c and d are images of another. a) concave back interface, c) convex back interface, b and d) nearly flat back interfaces and unequal front contact angles at the side walls

Figure 8: Variation in pressure difference across the length of a crawling bubble over time which is due to pinning and variation in the local surface conditions and contact angles

Figure 9: Comparison between the model's predictions and the measured pressures for the 6 sets of experiments. There could be a large difference between the concave and convex back model predictions.

Figure 10: Comparison between the measured pressure and the matching models' prediction. There are four irregular occurrences that have a slightly convex back interface but match the concave back model's prediction better.

Figure 11: Normalized models' predictions based on the measured pressure